Heliyon 8 (2022) e12478

Contents lists available at ScienceDirect

Heliyon

journal homepage: www.cell.com/heliyon

Research article

A fat fraction phantom for establishing new convolutional neural network to determine the pancreatic fat deposition

John Zhiyong Yang [a], Rinki Murphy [b,c,d,e,f], Jun Lu [a,f,g,h,*]

[a] Auckland Bioengineering Institute, The University of Auckland, Auckland, New Zealand
[b] School of Medicine, Faculty of Medical and Health Sciences, University of Auckland, Auckland, New Zealand
[c] Department of Surgery, Faculty of Medical and Health Sciences, University of Auckland, Auckland, New Zealand
[d] Auckland Diabetes Centre, Auckland District Health Board, Auckland, New Zealand
[e] Whitiora Diabetes Department, Counties Manukau District Health Board, Auckland, New Zealand
[f] Maurice Wilkins Centre for Biodiscovery, Auckland, New Zealand
[g] College of Food Engineering and Nutrition Sciences, Shanxi Normal University, Xi'an, 710119, Shanxi Province, China
[h] Key Laboratory of Forest Plant Ecology, Ministry of Education, Northeast Forestry University, Harbin 150040, China

ARTICLE INFO

Keywords:
MRI
Phantom
Intra-pancreatic fat
Automatic measurement
Machine learning

ABSTRACT

The determination of fat fraction based on Magnetic Resonance Imaging (MRI) requires extremely accurate data reconstruction for the assessment of pancreatic fat accumulation in medical diagnostics and biological research. In this study, the signal model of the oil and water emulsion was created with a 3.0 T field strength. We examined the quantification of the fat fraction from phantom and the intrapancreatic fat fraction using the techniques of magnetic resonance spectroscopy (MRS) and Iterative Decomposition with Echo Asymmetry and Least-Squares estimate (IDEAL) in magnetic resonance imaging (MRI). Additionally, we contrasted expert manual pancreatic fat assessment with MRS and IDEAL pancreatic fat fraction quantification. There was a strong connection between the true fat volume fraction and the fat fraction from IDEAL and MRS ($R^2 = 0.99$ and 0.99, respectively). For both phantom and in vivo measurements, Pearson's correlation and linear regression analysis were used. The findings of the in vivo assessment revealed a variable correlation between the pancreatic fat fraction MRI readings. We also used MR-opsy for manual pancreatic fat fraction segmentation since it read pancreatic fat fractions more accurately than IDEAL and MRS, which aided in the development of machine learning's ability to assess pancreatic fat automatically.

1. Introduction

A significant factor in determining the health risks associated with many metabolic disorders, such as obesity-related type 2 diabetes (T2D), many forms of malignancies, and major cardiovascular disease, is the distribution of adipose tissues, particularly visceral fat [1, 2, 3, 4]. Diabetes affects approximately 8.5% of the adult population worldwide [1], and is the key driver of early morbidity and mortality and health care costs [2]. The pancreas is a crucial organ regulates glucose homeostasis and energy metabolism. More and more clues in recent years suggests that T2D, the most common form of diabetes, is caused by reduction in pancreatic volume and physiological changes of visceral adipose tissues, especially ectopic fat deposition in the pancreas [3, 4, 5, 6, 7]. Thus, quantification of such pancreatic changes provides huge potential in terms of diagnosis and treatment to prevent T2D.

The precise detection and measurement of pancreatic fat deposition were challenging in the 20th century because of its retroperitoneal location in the body. However, within the last decade, accurate examination of the organs is now more accessible than ever because to advances in magnetic resonance imaging (MRI) and magnetic resonance spectroscopy (MRS) methods. MRI is now regarded as the most proper method for fat quantification due to its features of non-invasive and no ionizing radiation. Furthermore, MRI is sensitive for recognizing fat tissues from lean relay on chemical-shift properties and T_1 relaxation [8]. MRI allows not only the detection of the abnormalities of the pancreas structure but also the quantification of the dimension and composition of the organ based on various imaging parameters. On the other hand, MRS is generally regarded as the gold standard for the quantification of ectopic fat fraction in clinical trials. It has been used for the measurement of liver fat [9, 10], tissue composition [11], myocellular adipose tissue

* Corresponding author.
E-mail address: jeffjunlu@hotmail.com (J. Lu).

https://doi.org/10.1016/j.heliyon.2022.e12478
Received 16 February 2022; Received in revised form 20 May 2022; Accepted 13 December 2022

[12], and brain metabolites. Further, over the past 20 years, Iterative Decomposition with Echo Asymmetry and Least-Squares estimates (IDEAL) for MR images gradually became a sophisticated 3-dimensional (3D) imaging method based on a considerable increase in Dixon's reconstruction algorithms [13, 14]. IDEAL provides more reliable resonance offsets for separating fat and water phase images by optimizing their signal-to-noise ratio, which could have been difficult to calculate due to the impact of magnetic field nonuniformity [15].

The protons in water is separated from the main methylene groups $(–CH_2–)_n$ in triglyceride fatty acid chains at resonant frequencies around 3.4 ppm according to the chemical-shift principles in both IDEAL and MRS. In MRI machine. The unique character of water is reflected by a single spectral peak, whereas the fat tissue includes several continuous minor peaks, which represent methyl, olefinic, and carboxyl groups respectively. These peaks have similar difference chemical shifts compare with water [16]. Compared with MRS, the multi-fat-peak T_2*-IDEAL is a 3D images technique that presents spatial information and yields a fat-to-water (F/W) ratio by systematically analyzing the intravoxel dephasing and transverse relaxation effects on the specific MRI signals. These enabled a more accurate proton ratio measurement within both fat and water underlying tissues [17]. The latest 3D IDEAL is a water and fat (W and F) content separating method based on the Dixon technique [18].

However, given that the pancreas is relatively small and has varied and even hazy boundaries, quantifying fat accumulation inside such tiny organs remains difficult. Currently, the gold standard approach for quantifying pancreatic volume and fat deposition is the highly time-consuming manual operation on MR images by skilled professionals [19]. Al-Mrabeh et al. has established an efficient manual operation process called “MR-opsy” in terms of pancreatic fat fraction segmentation and claimed a good performance [20]. To improve the efficiency of the pancreatic measurement, we plan to establish a novel deep convolutional neural network (DCNN) closely imitate to the MR-opsy method to determine the pancreatic volume and pancreatic fat fraction from abdominal MRI. Segmentation on small intra organ such as pancreas by DCNN is a challenging mission as the pancreas structure under MRI are diverse due to the contamination from its surround organs [21]. Few previous studies were seen working on automatic pancreas segmentation on both CT and MRI, however, the outcomes of those studies can only estimate the pancreas volume but there are no studies up to date claiming the pancreatic fat fraction measuring function as the DCNN we plan to establish [21, 22, 23]. So, in this study, we were the first proposing a method for measuring the pancreatic fat deposition. This study described a phantom validation to 1) Set a scale reference for both clinical manual operation and future machine learning in terms of measuring pancreatic fat fraction; 2) Prospectively compare and evaluate the effectiveness of T_2*-IDEAL, MRS, and expert manual operation in terms of measuring the MRI-derived intrahepatic and intrapancreatic fat fractions; and 3) Described the potential algorithms for the novel DCNN that could be used for pancreatic fat segmentation based on the phantom result.

2. Materials and methods

2.1. Principles of T_2*-IDEAL and MRS

In this work, The IDEAL fat fraction was calculated from separating water signals (W) from fat ones (F) shown in equation (a):

$$Fat\ Fraction\ (FF_{IDEAL}) = \frac{F}{(W+F)} \times 100\%$$

We also employed the fat spectrum model [17] in IDEAL based on the signal model by the following equation (b):

$$s(t) = \left(W + F\sum a_i \bullet e^{j2\pi t(\Delta fi)}\right) e^{j2\pi t\Psi - \left(t/T_2^*\right)}$$

In this formula, s(t) represents for the signal in each voxel at time t; a_i and Δfi represents the relative amplitude and spectral frequency of F/W at the i^{th} peak respectively. j is the imaginary unit (i); and The signal's transverse relaxation and intravoxel dephasing are both represented by T_2*.

MRS data were acquired by the point-resolved spectroscopy method, which requires placing a single of a few cm^3 voxel in region-of-interest (ROI) of target organs. Obtaining signals through integration, MRS typically includes noise filtering, apodization, phase correction, and signal fitting of the peaks within the acquired spectrum, with each spectral peak area of interest being at 4.7 p.p.m. for W, at 1.3 p.p.m for F. The software of MRUI was utilized for spectral analysis. The fraction of fat in MRS was given in equation (c)

$$Fat\ Fraction\ (FF_{MRS}) = \frac{\text{area under peaks of fat}}{\text{area under peaks of both fat and water}} \times 100\%$$

2.2. Phantom study

Using vegetable (soy) oil, distilled water, and undoped water, we produced a homogeneous emulsion series in order to evaluate the accuracy of each type of quantification result. Lecithin (1% by weight from Sigma) and fat volume fractions ranging from 0% to 100% were added to 100-ml bottles. The emulsions were stabilised by adding sodium dioctyl sulfosuccinate salt and agar gel (3% of the weight). The emulsions were carefully spun over a heat plate to achieve an even dispersion of the suspension before being gradually cooled to room temperature. The bottles were then placed in a container filled with solid agar, and the MRI test was performed using the following parameters: Repetition time: 10 ms, echo times: 2, 4, 6, 8, 3.2, 3.6, and 4.0 ms, flip angle: 5°, receiver bandwidth: 125 kHz, in-plane spatial resolution: 2 mm, slice lengths: 8 mm, and single signal average. On ten emulsions with a fat content of 10–100% fat, the same scan settings of repetition time = 4s, echo time = 23ms, and bandwidth = 2.5kHz were used.

2.3. Clinical participants for validation

The clinical research received approval from the Health and Disability Ethics Committee (HDECs), Auckland and followed all informed consent guidelines. The abdominal MR images of 16 healthy participants were selected for the study (6 males, 10 females, age range 20–55 years, the details of participants were summarized in Table 1). All those who took part in the study were given their informed consent. Exclusion criteria

Table 1. Summary of anthropological details of 16 participants in this study.

Participant ID	Gender	Age	Weight (kg)	Height (m)	BMI	Ethnicity
1	Male	20	71.5	1.82	21.6	NZ European
2	Male	28	88.8	1.79	27.7	NZ European
3	Male	35	106.7	1.88	30.2	NZ European
4	Male	32	89.7	1.75	29.3	Pacific Islander
5	Male	22	78.7	1.83	23.5	Pacific Islander
6	Male	55	93.4	1.69	32.7	Māori
7	Female	38	86.4	1.58	34.6	Māori
8	Female	43	94.3	1.77	30.1	NZ European
9	Female	52	83.8	1.68	29.7	NZ European
10	Female	48	75.7	1.72	25.6	NZ European
11	Female	21	81.1	1.56	33.3	Pacific Islander
12	Female	29	74.7	1.67	26.8	Pacific Islander
13	Female	33	68.2	1.55	28.4	Pacific Islander
14	Female	39	46.2	1.58	18.5	Asian
15	Female	46	59.1	1.65	21.7	Asian
16	Female	32	62.7	1.63	23.6	Asian

included being on regular drugs, having a history of cancer, diabetes, celiac disease, cystic fibrosis, chronic pancreatitis, being pregnant, or exhibiting upper abdomen pain and nausea. They also had no endocrine abnormalities or a history of acute viral or inflammatory disorders requiring medical evaluation or treatment in the three months prior to the research date. Participants were also disqualified if they had any general MRI contraindications (such as metallic foreign body or electronic device implantation).

2.4. MR imaging protocol

We booked a 3.0 T MAGNETOM Skyra scanner at the Center of Advanced MRI (University of Auckland) and associated all participants in this study got MRI scans (Siemens, Erlangen, Germany). Eight-channel abdominal arrays with receive-only capability were used to collect participant data. In this work, the Dixon sequence for axial T_1-weighted volumetric interpolated breath-hold imaging was applied. Each subject had a single axial 3D IDEAL spoiled-gradient-echo capture encompassing the right lobe of the liver and pancreas. A total of 12 slices were acquired, and the parameters for MRI imaging were established similarly to those for the phantom study with the exception that resolution in-plane was set at a range of 2–2.75 mm depending on body habitus. Six echoes spacing 0.8ms were acquired in total with the first echo between 1.0-1.5 ms. The IDEAL scans were conducted under giving the participants instruction of 20s breath-hold section. The measurements, which were reflected in the relative proton density fat fraction (PDFF), were based on T_1 bias, T_2* decay, noise bias, and fat depostion [24]. The fat content measurement was performed and archived by picture archiving and communication system (PACS) with MRI workstations. The output was automatically determined by stacking with quantitative coding of degrees of grey values in PDFF. Each MRS scan consumed 3–4 min with no breath-holding. MRS was conducted on the pancreas with the same parameters as the phantom, eight signal averages, and no water suppression. In order to avoid including any visceral fat surrounding the pancreas when measuring the liver and pancreas, the voxel was placed inside the organs. The volume located in hepatic and pancreatic fat content were $30 \times 30 \times 30$ mm^3 and $15 \times 15 \times 15$mm [3], respectively (Figure 1 a.b).

2.5. MR image analysis

Fat content in both pancreas and liver was measured by experienced radiologist in MRI center.

2.5.1. Pancreatic fat fraction (PFF)

Utilizing the customized off-line workstation, the areas of focus region were circled to determine the pancreatic fat concentration (Syngo.via, Siemens Healthcare, Erlangen, Germany). Throughout many MRI slices, each ROI spanned a about 100 mm^{2}area into the pancreatic head, body, and tail (Figure 1c).

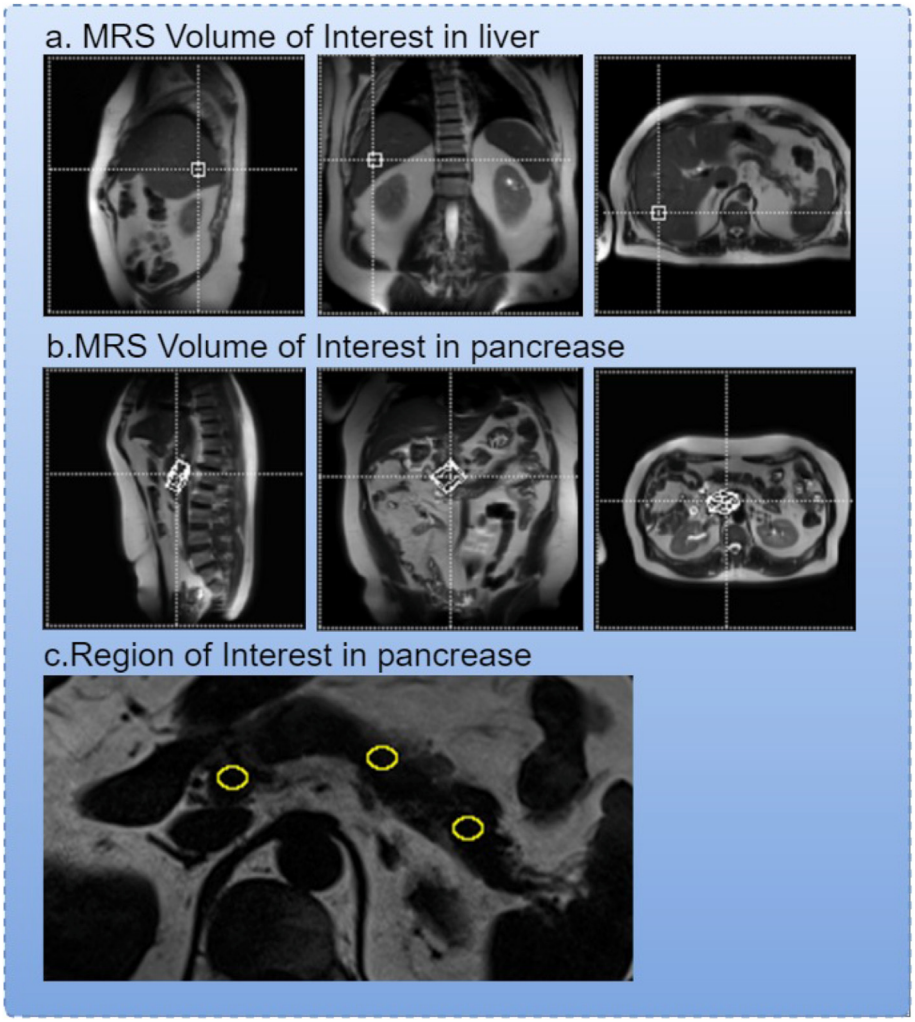

Figure 1. Assessment of hepatic and pancreatic fat content in MRI. a.) The volume of interest located in liver, b.) The volume of interest located in pancreas, c.) The region of interest (yellow circle) on MRI fat image.

2.5.2. Hepatic fat fraction (HFF)

A single axial slice at the plane near the portal vein was used to estimate the amount of hepatic fat based on the acquired multi-echo Dixon images of the upper abdomen. To avoid including any apparent extra- and intra-hepatic arteries, the ROI was meticulously circled into the liver parenchyma to quantify the amount of hepatic fat present.

2.5.3. Post manual pancreatic fat fraction segmentation

The pancreas fat fraction was also segmented manually by experts followed the description of MR-opsy method described by Al-Mrabeh et al. [20, 25, 26]. Using Image J to measure the percentage fat for all highlighted RoiSets within the ROI manager. The finial fat percentage was obtained by excluding values less than 1% and over 20% on excel spreadsheet generated by Histogram on Image J. The process of segmentation was shown in Figure 2. For the fat deposition in pancreas, we only reserved the pixel with fat values of 1%–20% in order to minimize inclusion of non-parenchymal tissues [20]. We compared the results of this method with the ones derived from MRS and IDEAL.

2.6. Data and statistical analysis

In the phantom investigation, linear regression was used to evaluate the fat fractions derived from IDEAL and MRS to the genuine fat volume fraction. Pixel length was converted into millimeters for further application on manual operation and machine learning. From the in vivo studies, expert manually derived pancreas fat fraction (PFF_{MANUAL}) based on phantom scale was compared with the methods of IDEAL (PFF_{IDEAL}) and MRS (PFF_{MRS}) for validation. In those comparisons, Pearson's correlation coefficient (r) and linear correlation were used. The linear regression was analyzed by identifying the gradient difference derived by the t-test. Box-and-whisker plots were drawn from paired t-tests to test whether there were statistical differences among methods. For the in vivo experiments, the 95% confidence intervals, and $P < 0.05$ was used to assert statistical significance.

2.7. Algorithm design for novel DCNN

2.7.1. The overview of the new DCNN

For building up DCNN, we plan to collect more MRI data from previous research projects and recruit more participants from our current clinical study. The MR images include opposite phase series, water and fat images. We plan to use manual labelled water phase pancreas MR images to establish the new DCNN that segmented pancreas automatically.

The hyperparameters of new DCNN will be tuned by Bayesian Optimization algorithm [27] inputting the data we currently have, containing the total number of neurons, the activation function, the optimizer, the learning rate, the batch size, the epochs, and the total number of layers. This function can be achieved by package of Keras in Python, which is

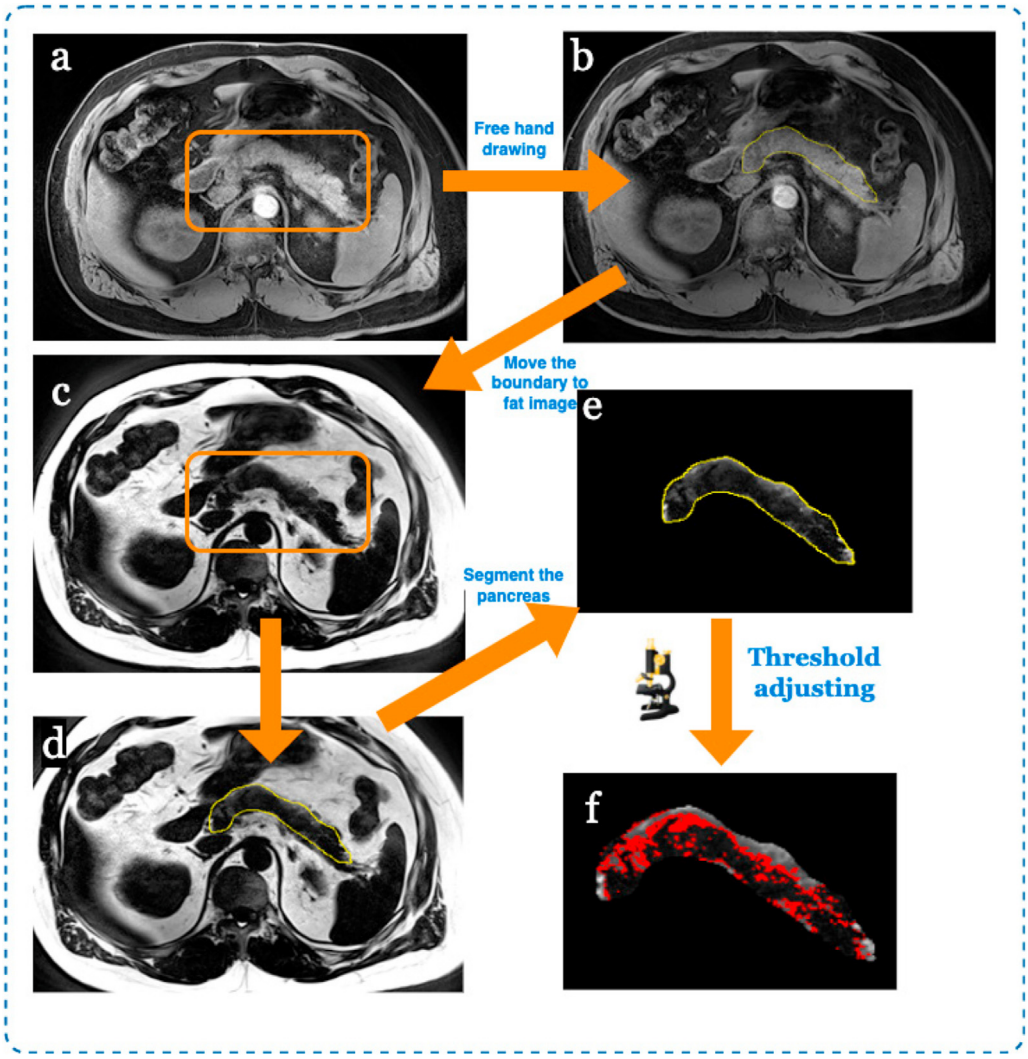

Figure 2. The manual MRI segmentation process for pancreatic fat fraction. a.) the water image with centered pancreas. b.) the corresponding fat image with centered pancreas. c.) manual segmentation of the pancreas. d.) transfer of the pancreas boundary from water image to fat image. e.) pancreas segmented from the fat image. f.) threshold adjusted until most of the inner pancreas pixels were covered. Using Image J to measure the percentage fat for all highlighted RoiSets within the ROI manager. The finial fat percentage was obtained by excluding values less than 1% and over 20% on excel spreadsheet generated by Histogram on Image J.

built on top of Tensorflow. The overview of the DCNN was summarized in Figure 3.

The pancreas volume can be calculated by accumulating the multiplication of each pancreatic area and thickness of MRI slice (3mm). We enable the DCNN this function via the Cavalieri equation [28].

$$Volume\ in\ vivo = \sum Volumes\ of all\ pancreatic\ slices$$

2.7.2. The erosion process

After training and validating of DCNN, we will use it to pick up the pancreas from MR fat images with inversed grey values of water images. In order to reduce the impact of the extra pixel form boundary detection, we employed erosion algorithm in OpenCV to remove them. Erosion is one of the important morphological operations. It computes a local minimum over the area of given kernel, which can be adjusted until we got satisfy segmenting result. The equation of erosion algorithm was summarized as:

$$X\ \Theta\ B = X - b = \{z: (B + z) \subseteq X\}$$

Where X Θ B is defined as the opening off set X by structural element B, the erosion of X by B is the set of any b such that B, translated by b, is contain X.

2.7.3. Pancreatic fat measurement

Traditional manual pancreatic fat segmentation defines areas of interest (ROI) throughout the whole pancreas in order to lessen inter- and intra-observer variability, and findings were reported by the program of Image J with automatically analyzed pixel percentage. The pixels that represented histologically confirmed blood arteries, ducts, or visceral fat and had fat percentage values between <1% and >20% were carefully eliminated. We will enable our CNN the same feature as manual operation for accumulating the corresponding fat pixels. The information of fat percentage was shown by the different brightness of pixels from the phantom result, which can be turned into digital signal by the Pillow algorithm in Python for the machine learning. The pixels of fat are to be accumulated and pixels with values of <1% and >20% will be excluded.

3. Results

3.1. Summary of phantom study results

Figure 4 provided a summary of the phantom experiment's findings, where the IDEAL fat gradient heatmaps for separated water, fat, and fat fraction are displayed. The gradient of each phantom emulsions was plotted linearly and compared with the true fat volume fraction. Figure 4d demonstrated the high correlation between the real fat volume fraction and the fat fraction from IDEAL and MRS (slope = 0.99, R^2 = 0.99, $P < 0.001$) in IDEAL and (slope = 0.95, R^2 = 0.99, $P < 0.001$) in MRS. It was less biased in MRS when compared to the zero-intercept (0.69). The reason for this is probably because in IDEAL, the magnitude values of F and W were employed in the fat fraction operation in Eq. (a) to balance the effects of the inherent noise in the separated fat-water images and the phase errors caused by eddy currents from the magnet hardware. It was also claimed that the IDEAL approach is more accurate at assessing fat content and more dependable at separating fat from water. The pixel length was converted to length in millimeter through measuring tools in the app of Image J. We measured the real size of the diameter (42mm) of the bottle by tape and, the result matched the one received from the software. We also measure the length of the container for reference shown in Figure 4c. The result was concluded in the table, and the average convert ratio was 0.76. The pixel to digital information conversion was done by python pillow algorithm and the brightness gradient was generated on machine shown in Figure 4e.

3.2. HFF results of IDEAL and MRS from patients

The HFF results from two subjects that read from both IDEAL and MRS was illustrated in Figure 5a. One subject (patient 16) had a lean liver with the HFF_{IDEAL} reading of 5.32% and HFF_{MRS} reading of 4.94%, respectively. The other (patient 3) had a relative fattier liver with the HFF_{IDEAL} reading of 34.28% and HFF_{MRS} reading of 35.61%, respectively. Figure 5.a summarized the paired t-test result between the HFF_{IDEAL} and the HFF_{MRS} from all 16 MRI scans. The outcome indicated that the two measurements did not differ significantly ($P = 0.239$). The Pearson's correlation result ($P < 0.01$) showed that a strong agreement between the HFF_{IDEAL} and the HFF_{MRS}. The regression results further proved that the fat fraction readings from both MRS and IDEAL were highly matched. The slope was 0.9787, the intercept was 0.0632, the R^2 was 0.99, respectively.

3.3. Validation of PFF results from patients

3.3.1. PFF results of IDEAL and MRS from patients

The PFF results from two subjects that read from both IDEAL and MRS. Participant 14 had a lean pancreas with the PFF_{IDEAL} reading of 4.32% and PFF_{MRS} reading of 6.88%, respectively. Participant 11 had a relative fattier pancreas with the PFF_{IDEAL} reading of 14.23% and PFF_{MRS} reading of 22.36%, respectively. Figure 5b illustrated the paired t-test result between the PFF_{IDEAL} and the PFF_{MRS} from all 16 MRI scans. The result showed that there was a significant difference between the two readings ($P < 0.02$). The Pearson's correlation result ($P < 0.05$) indicated that there was a relatively similar trend between the PFF_{IDEAL} and the PFF_{MRS}. However, the regression results showed that the fat fraction readings from IDEAL and MRS were not agreed with each other. The slope was 0.5884, the intercept was 0.7324, the R^2 was 0.92, respectively.

3.3.2. PFF validation by manual operation

The PFF_{IDEAL} and PFF_{MRS} were compared with the manually derived PFF results, which were shown in Figure 6 a.b. The regression correlation between PFF_{MANUAL} and PFF_{MRS} was 0.2703 with the interception of 1.4005, and R^2 of 0.7397. The regression correlation between PFF_{MANUAL}

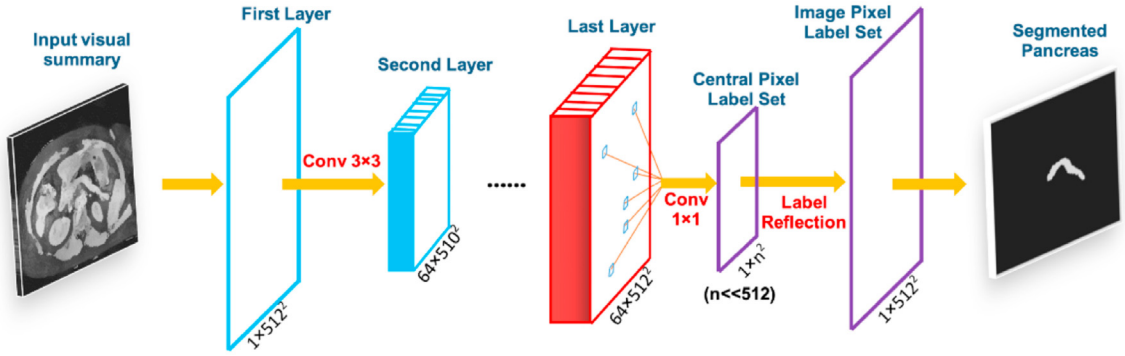

Figure 3. The overview of the new DCNN for segmenting the pancreas from MR image.

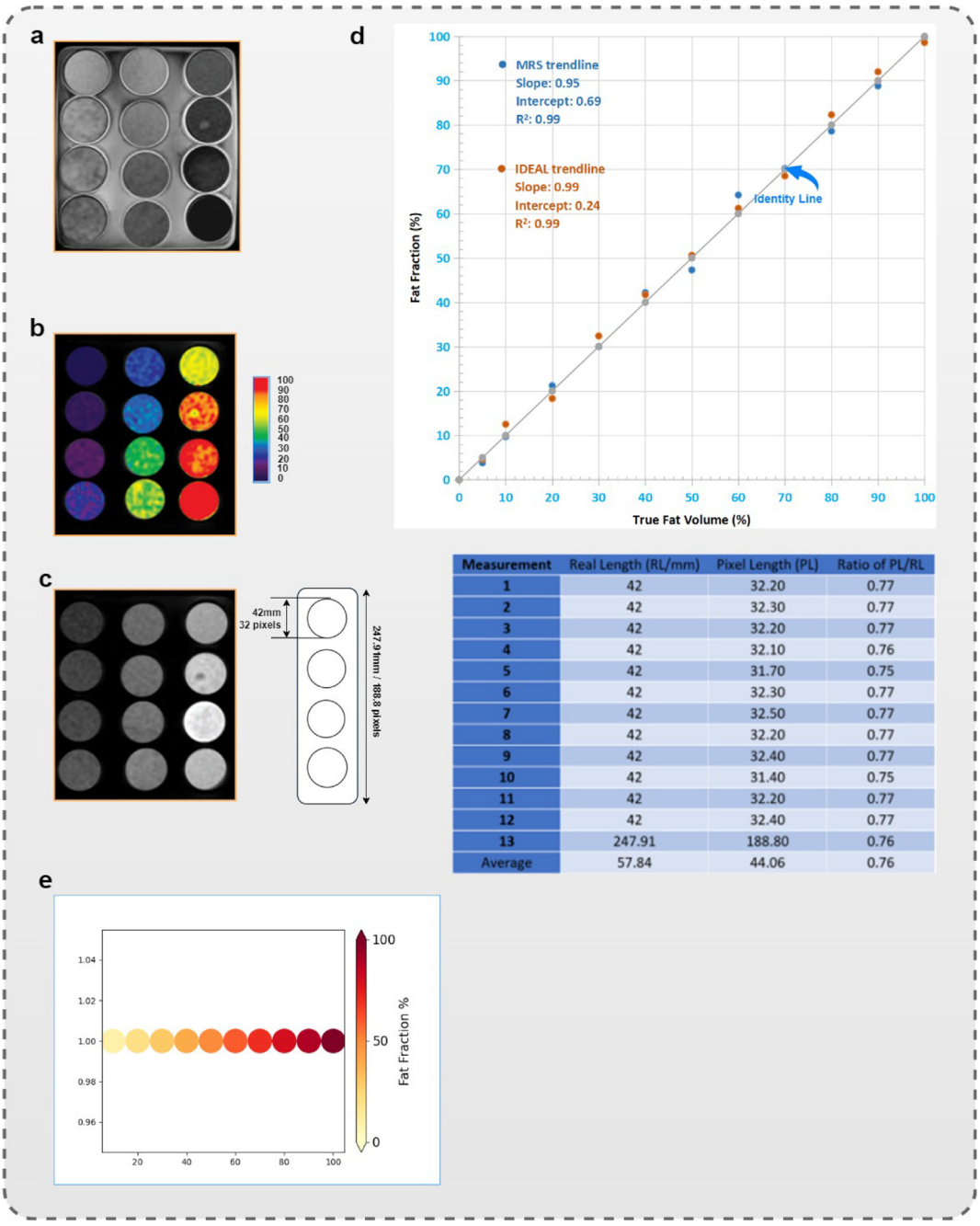

Measurement	Real Length (RL/mm)	Pixel Length (PL)	Ratio of PL/RL
1	42	32.20	0.77
2	42	32.30	0.77
3	42	32.20	0.77
4	42	32.10	0.76
5	42	31.70	0.75
6	42	32.30	0.77
7	42	32.50	0.77
8	42	32.20	0.77
9	42	32.40	0.77
10	42	31.40	0.75
11	42	32.20	0.77
12	42	32.40	0.77
13	247.91	188.80	0.76
Average	57.84	44.06	0.76

Figure 4. Phantom results from oil-water emulsion. a.) the water image. b.) the heatmap of fat fraction gradient. c.) the fat images with the result of pixel to millimeter length conversion measurement. d.) correlation between real fat volume fraction and the mean fat fraction derived by MRS and IDEAL. e.) Fat fraction gradient heatmap generated by python pillow algorithm for machine learning.

and PFF_{IDEAL}L was 0.4516 with the interception of 1.1308, and R^2 of 0.7738. The regression gradient of both readings of PFF_{MRS} and PFF_{IDEAL} and PFF_{MANUAL} sloped away from the identity line, which means the PFF readings from the artificial method was not in agreement with the MRI machine. The t-test result also showed there was a significant difference between PFF_{MANUAL} and PFF_{MRS} with $p < 0.01$ and between PFF_{MANUAL} and PFF_{IDEAL} with $p < 0.01$. The general pancreatic fat deposition range was reported as 1.8%–10.4% with a mean of 4.5% [29], which was shown on the box-plot graph by a dashed line.

3.4. CNN parameters from phantom study

By running Bayesian optimization, we evaluated the optimum of hyperparameters and layers of DCNN by inputting our limited MR images. The batch size was 726, epochs was 43.5, learning rate was 0.037, neurons was 28.6, and the optimizer was 0.73. We converted the pixel length (PL) to real length in millimeters (RL) for future study. The conversion ratio of PL and RL was averaged as 0.76. The fat fraction information has also been converted into digital signal and applied into the novel DCNN (Figure 4 e) and ready to use.

The new DCNN was trained by limited numbers of MR images (200) from the patients, and the preliminary results was shown in Figure 7. The best segmentation result is close to the expert. However, most of the images were out of the segmenting accuracy due to the limited training set. The evaluation parameters were summarized in Figure 7b. We trained the machine to segment the pancreas from fat MR images and by applying the erosion algorithm, we can successfully label the potential fat pixels.

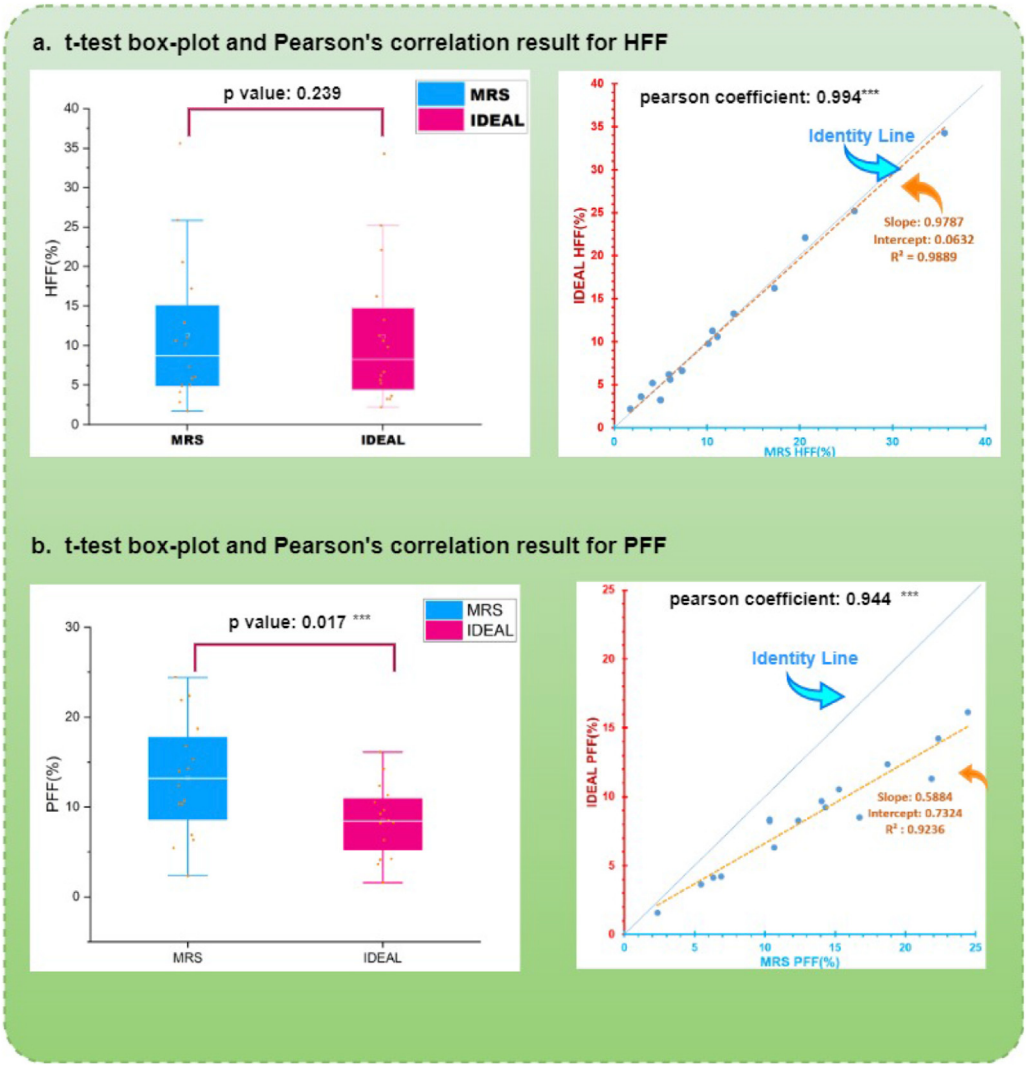

Figure 5. Pancreatic fat fractions (PFF) and Hepatic fat fractions (HFF) results from both MRS and IDEAL. a.) t-test box-plot result showed that the HFF of IDEAL was similar from PFF of MRS with p value of 0.239 and Pearson's correlation and regression of HFF derived by IDEAL and MRS were also shown in 16 studies. b.) t-test box-plot result showed that the PFF of IDEAL was significantly different from PFF of MRS with p value of 0.017 and Pearson's correlation and regression of PFF between IDEAL and MRS were also shown in 16 studies.

4. Discussion

In our study, we compared and evaluated the effectiveness of IDEAL and MRS in measuring the MRI-derived PFFs. The resulting PFF_{IDEAL} and PFF_{MRS} data for each processing approach were compared with the manually derived PFF data to assess the efficiency of these pancreatic fat fraction quantification methods.

In our phantom study using a set of emulsion standards, we have demonstrated that the underlying fat volume fraction was well associated with both the MRS and IDEAL fat fractions (Figure 4). Other studies have also verified this robust relationship [24, 30]. In the in vivo experiment for transverse relaxation and intravoxel dephasing (T_2, T_2*), the IDEAL algorithm utilized six echoes [31]. We utilized a single echo time of 23ms for our MRS protocol because the T_2 correction required additional echo times that may have been avoided at the expense of the scan period for MRS. The results showed that the HFF_{IDEAL} and HFF_{MRS} had great agreement, while the PFF measurement only had a reasonable correlation between the PFF_{IDEAL} and PFF_{MRS} (Figure 5) since the values were statistically different. The MRS estimates were almost generally higher than the IDEAL values. We also noticed that in our data, there were some extremely large MRS estimates up to 62.8% due to intravoxel field inhomogeneity in the MRS voxel. Hence this MRS data was abandoned. Such aberrancies did not appear in IDEAL readings.

The poor PFF correlation between each reading may be attributed to two reasons. Firstly, MRS voxel placement requires operator expertise in order to avoid the pancreatic ducts, which can happen because the pancreas is such a small, elongated shaped organ that is frequently difficult to localize clearly. On localizer images that were scanned after the patients were positioned inside the MRI tunnel, voxel prescription is carried out. Since the pancreas MRS was performed after the localizer by a few minutes, there may have been a spatial mismatch between the specified voxel and the physiological structure as a result of the patients' slight mobility during that period. Secondly, respiration caused the abdominal organs to shift readily [32]. The movement of the diaphragm during inhalation and expiration causes the pancreas to move along the superior-inferior axis by roughly 15 mm, which could cause fat signal contamination due to the large amount of visceral fat around the pancreas and reflect on MRS spectra. As a result of the liver's relatively big and uniform structure, which allows for confident positioning within the organ throughout the respiration cycle, voxel placement is significantly simpler for the liver.

In terms of PFF measurements, IDEAL-MRI outperformed MRS. During the patient's breath-hold period, the IDEAL functions clearly and doesn't call for a high level of operator voxel placement proficiency. Additionally, following data gathering, IDEAL images were rebuilt, and fat fraction was calculated on the scanner host computer for an additional 2–3 min. The manual segmentation of HFF and PFF was operated on fat fraction images directly, which helps to avoid a large amount of background noise of vessels and non-fat structures. This advantage was also recognized by parallel validation studies that included large patient cohorts [24, 33, 34]. However, IDEAL also has intrinsic limitations. Firstly, IDEAL depends on the respiration restriction of the patient, which is not

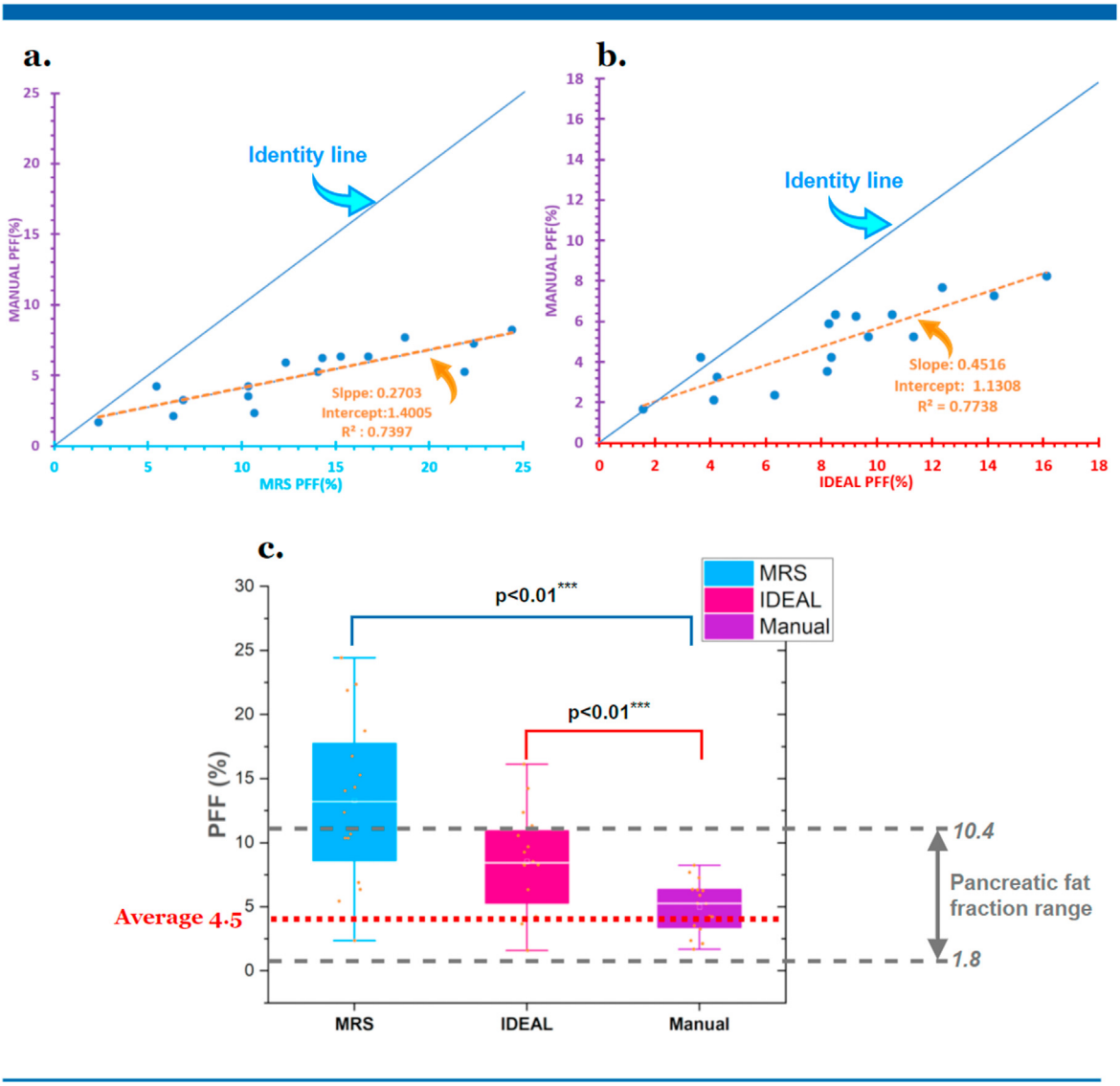

Figure 6. Correlation of the manually and machine derived PFF. a.) Regression of MRS PFF and manually derived PFF b.) Regression of IDEAL PFF and manually derived PFF c.) T-test box-plot results between MRS PFF, IDEAL PFF and Manually derived PFF. The general pancreatic fat fraction range and mean value were noted with dash line.

always realistic in certain patients. Secondly, based on Eq (b), to build a precise model of the fat spectrum, we must assign the values of Δfi and a_i, which are determined by subcutaneous adipose tissue. If the signal of triglycerides in organs differs greatly from that of subcutaneous fat tissue, inaccuracies may appear. Thirdly, the values of T_2* were assigned for both water and fat components, which should have been adopted. This can be addressed by enlarging the acquisition echoes; however, long time operation also takes potential inaccuracies.

In this study, the manual PFF method was employed to compare the difference in performance between IDEAL and MRS and to get a more accurate PFF reading. We employed MR-opsy method that using the Image J Polygon tool to cycle the ROI in the pancreatic parenchymal tissue. These index regions were selected carefully in order to stay away from any potential contamination of the visceral fat nearby (Figure 2). The threshold was adjusted until satisfactory fat pixels were exposed. Then pixels within the threshold range of between 1% and 20% were selected, measured and converted into fat percentage by Image J tool. The total area of the pancreas on each slice were obtained and summed. The ratio of the pancreatic fat area and total pancreas area were noted and counted into the PFF_{MANUAL}. Based on the result in Figure 6c, in terms of PFF reading. The results were exactly laid on the reported general pancreatic fat fraction range (1.8%–10.4% with the mean of 4.5%) [35].

We preliminary evaluated the performance of the DCNN. It is with feasibility to copy the manual segmentation method onto machine. Based on the comparison between different fat fraction measuring method, we solidify the idea that machine learning can significantly improve the efficiency and accuracy in terms of obesity and other types of metabolic diseases diagnosing. The knowledge acquired from our study will be utilized in our future work to focus on the establishment of MRI quantification and to develop machine learning systems to determine the pancreatic fat depositions in order to link these measurements with metabolic disorders.

However, there are major limitations of the manual method. Firstly, there isn't a non-invasively gold standard for measuring fat just in the parenchymal tissue of the pancreas. With the development of imaging techniques, in the near future, it is possible to have an superior method that optimized images with better differentiation the ductal or tiny vascular structures from parenchymal tissue, such as the T_2-SPAIR sequence [36]. Secondly, the resolution of pancreas imaging in a shorter period need to be improved. The breath-hold duration was restricted to a

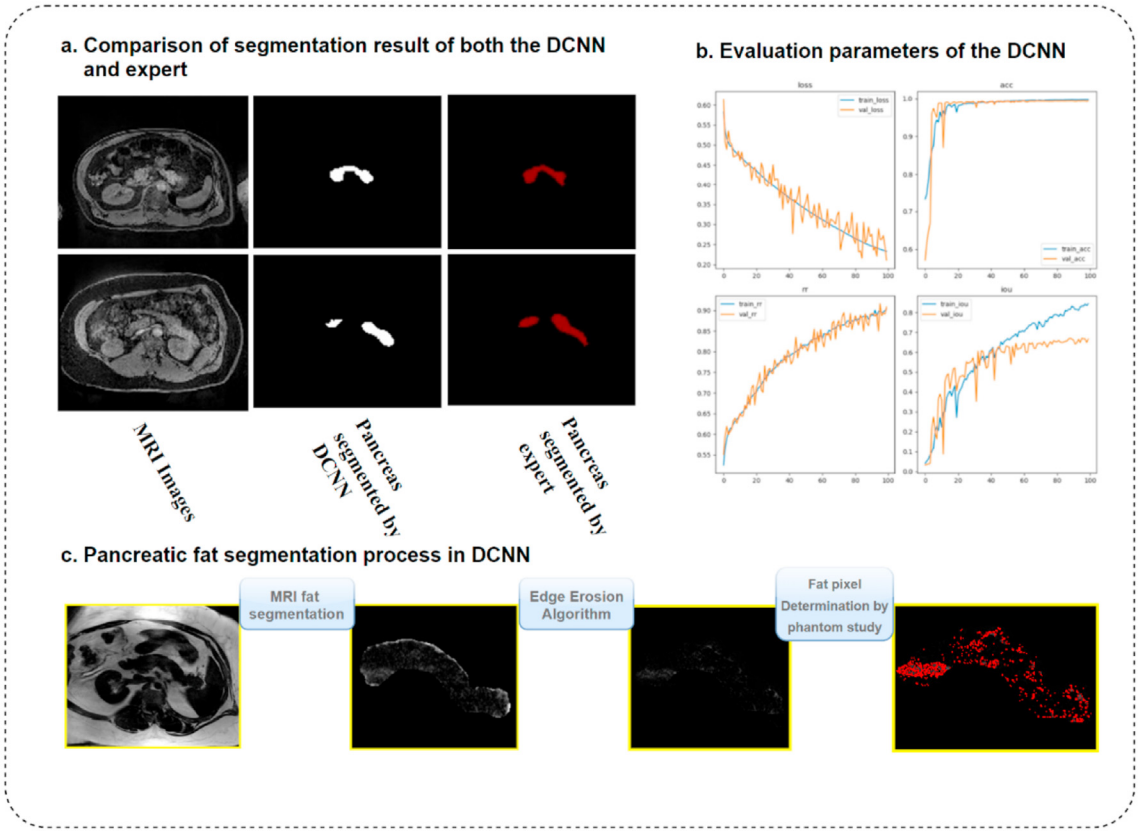

Figure 7. The preliminary results of the temporary DCNN trained by 200 MR images a.) Comparison of segmentation best result of both the DCNN and expert b.) Evaluation parameters of the DCNN c.) Pancreatic fat segmentation process shown in DCNN.

lot of patient groups, which lowered the resolution of the images. Sparse scanning techniques may fill the gap soon [37]. Thirdly, the patients were in different age, gender, and ethnicity groups, which may take uncertainties in terms of intra organ fat deposition. However, different methods were applied on measuring the fat fraction for each participant, which formed comparison. Fourthly, due to the limitation of small data set, we cannot draw any conclusion on our newly built DCNN. However, our ideas were feasible to be achieved by machine, which means the artificial method remains useful because the threshold adjusting can exclude the areas of visceral fat invasion effectively and the accuracy can be improved dramatically by examining the detail of the pancreas when conducting the selection of ROI.

5. Conclusion

In conclusion, the sampling technique has a substantial impact on the pancreas' ability to quantify fat via MRI. The MRI measurement for water/fat decomposition is a valuable method for hepatic and pancreatic fat fraction quantification. Based on our research, we have shown that the manual pancreatic fat fraction derived approach has a significant advantage as a pancreatic fat quantification tool. We recommend this approach as a useful machine learning technique for automating the fat quantification of pancreatic fat fractions for clinical risk assessment of metabolic disease and research application.

Declarations

Author contribution statement

John Zhiyong Yang: Conceived and designed the experiments; Performed the experiments; Analyzed and interpreted the data; Wrote the paper.

Rinki Murphy: Conceived and designed the experiments; Wrote the paper.

Jun Lu: Conceived and designed the experiments; Contributed reagents, materials, analysis tools or data; Wrote the paper.

Funding statement

Prof. Jun Lu was supported by Maurice Wilkins Centre for Molecular Biodiscovery [MWC327].

Data availability statement

Data included in article/supp. material/referenced in article.

Declaration of interests statement

The authors declare no conflict of interest.

Additional information

No additional information is available for this paper.

References

[1] S. Cheng, J.M. Massaro, C.S. Fox, et al., Adiposity, cardiometabolic risk, and vitamin D status: the framingham heart study, Diabetes 59 (1) (2010) 242–248.
[2] P.O. Coe, S.R. Williams, D.M. Morris, et al., Development of MR quantified pancreatic fat deposition as a cancer risk biomarker, Pancreatology 18 (4) (2018) 429–437.
[3] R.G. Singh, A. Cervantes, J.U. Kim, et al., Intrapancreatic fat deposition and visceral fat volume are associated with the presence of diabetes after acute pancreatitis, Am. J. Physiol. Gastrointest. Liver Physiol. 316 (6) (2019) G806–G815.

[4] U.L. Sreedhar, S.V. DeSouza, B. Park, M.S. Petrov, A systematic review of intra-pancreatic fat deposition and pancreatic carcinogenesis, J. Gastrointest. Surg. 24 (11) (2020) 2560–2569.

[5] M. Ashwell, P. Gunn, S. Gibson, Waist-to-height ratio is a better screening tool than waist circumference and BMI for adult cardiometabolic risk factors: systematic review and meta-analysis, Obes. Rev. 13 (3) (2012) 275–286.

[6] W. Shen, Z. Wang, M. Punyanita, et al., Adipose tissue quantification by imaging methods: a proposed classification, Obes. Res. 11 (1) (2003) 5–16.

[7] S. Martin, E.P. Sorokin, E.L. Thomas, et al., Estimating the effect of liver and pancreas volume and fat content on risk of diabetes: a Mendelian randomization study, Diabetes Care 45 (2) (2022) 460–468.

[8] R. Longo, P. Pollesello, C. Ricci, et al., Proton MR spectroscopy in quantitative in vivo determination of fat content in human liver steatosis, J. Magn. Reson. Imag. 5 (3) (1995) 281–285.

[9] H. Kim, S.E. Taksali, S. Dufour, et al., Comparative MR study of hepatic fat quantification using single-voxel proton spectroscopy, two-point dixon and three-point IDEAL, Magn. Reson. Med.: An Official Journal of the International Society for Magnetic Resonance in Medicine 59 (3) (2008) 521–527.

[10] C. Thomsen, U. Becker, K. Winkler, P. Christoffersen, M. Jensen, O. Henriksen, Quantification of liver fat using magnetic resonance spectroscopy, Magn. Reson. Imag. 12 (3) (1994) 487–495.

[11] J. Machann, O.P. Bachmann, K. Brechtel, et al., Lipid content in the musculature of the lower leg assessed by fat selective MRI: intra-and interindividual differences and correlation with anthropometric and metabolic data, J. Magn. Reson. Imag.: An Official Journal of the International Society for Magnetic Resonance in Medicine 17 (3) (2003) 350–357.

[12] J. Ren, I. Dimitrov, A.D. Sherry, C.R. Malloy, Composition of adipose tissue and marrow fat in humans by 1H NMR at 7 Tesla, J. Lipid Res. 49 (9) (2008) 2055–2062.

[13] P.A. Hardy, R.S. Hinks, J.A. Tkach, Separation of fat and water in fast spin-echo MR imaging with the three-point Dixon technique, J. Magn. Reson. Imag. 5 (2) (1995) 181–185.

[14] Q.S. Xiang, Two-point water-fat imaging with partially-opposed-phase (POP) acquisition: an asymmetric Dixon method, Magn. Reson. Med.: An Official Journal of the International Society for Magnetic Resonance in Medicine 56 (3) (2006) 572–584.

[15] S.B. Reeder, A.R. Pineda, Z. Wen, et al., Iterative decomposition of water and fat with echo asymmetry and least-squares estimation (IDEAL): application with fast spin-echo imaging, Magn. Reson. Med.: An Official Journal of the International Society for Magnetic Resonance in Medicine 54 (3) (2005) 636–644.

[16] G. Brix, S. Heiland, M.E. Bellemann, T. Koch, W.J. Lorenz, MR imaging of fat-containing tissues: valuation of two quantitative imaging techniques in comparison with localized proton spectroscopy, Magn. Reson. Imag. 11 (7) (1993) 977–991.

[17] H. Yu, A. Shimakawa, C.A. McKenzie, E. Brodsky, J.H. Brittain, S.B. Reeder, Multiecho water-fat separation and simultaneous R estimation with multifrequency fat spectrum modeling, Magn. Reson. Med.: An Official Journal of the International Society for Magnetic Resonance in Medicine 60 (5) (2008) 1122–1134.

[18] W.T. Dixon, Simple proton spectroscopic imaging, Radiology 153 (1) (1984) 189–194.

[19] M. Borga, MRI adipose tissue and muscle composition analysis—a review of automation techniques, Br. J. Radiol. 91 (1089) (2018), 20180252.

[20] A. Al-Mrabeh, K.G. Hollingsworth, S. Steven, D. Tiniakos, R. Taylor, Quantification of intrapancreatic fat in type 2 diabetes by MRI, PLoS One 12 (4) (2017), e0174660.

[21] Y. Yan, D. Zhang, Multi-scale U-like network with attention mechanism for automatic pancreas segmentation, PLoS One 16 (5) (2021), e0252287.

[22] S.-H. Lim, Y.J. Kim, Y.-H. Park, D. Kim, K.G. Kim, D.-H. Lee, Automated pancreas segmentation and volumetry using deep neural network on computed tomography, Sci. Rep. 12 (1) (2022) 1–9.

[23] H. Kumar, S.V. DeSouza, M.S. Petrov, Automated pancreas segmentation from computed tomography and magnetic resonance images: a systematic review, Comput. Methods Progr. Biomed. 178 (2019) 319–328.

[24] S. Reeder, C. Hines, H. Yu, C. McKenzie, J. Brittain, On the Definition of Fat-Fraction for in Vivo Fat Quantification with Magnetic Resonance Imaging, 2009, p. 211.

[25] J.Z. Yang, D. Dokpuang, R. Nemati, et al., Evaluation of ethnic variations in visceral, subcutaneous, intra-pancreatic, and intra-hepatic fat depositions by magnetic resonance imaging among New Zealanders, Biomedicines 8 (6) (2020) 174.

[26] A. Al-Mrabeh, C. Peters, K.G. Hollingsworth, R. Taylor, Measurement of intraorgan fat and hepatic output of triglycerides in human type 2 diabetes by magnetic resonance and intralipid infusion techniques, STAR protocols 2 (1) (2021), 100355.

[27] M. Pelikan, Bayesian Optimization Algorithm. Hierarchical Bayesian Optimization Algorithm, Springer, 2005, pp. 31–48.

[28] B. Sahin, M. Emirzeoglu, A. Uzun, et al., Unbiased estimation of the liver volume by the Cavalieri principle using magnetic resonance images, Eur. J. Radiol. 47 (2) (2003) 164–170.

[29] V.W.-S. Wong, G.L.-H. Wong, D.K.-W. Yeung, et al., Fatty pancreas, insulin resistance, and β-cell function: a population study using fat-water magnetic resonance imaging, Official journal of the American College of Gastroenterology| ACG 109 (4) (2014) 589–597.

[30] M. Bydder, T. Yokoo, G. Hamilton, et al., Relaxation effects in the quantification of fat using gradient echo imaging, Magn. Reson. Imag. 26 (3) (2008) 347–359.

[31] P. Sharma, D.R. Martin, N. Pineda, et al., Quantitative analysis of T2-correction in single-voxel magnetic resonance spectroscopy of hepatic lipid fraction, J. Magn. Reson. Imag.: An Official Journal of the International Society for Magnetic Resonance in Medicine 29 (3) (2009) 629–635.

[32] K. Nehrke, P. Bornert, D. Manke, J.C. Bock, Free-breathing cardiac MR imaging: study of implications of respiratory motion—initial results, Radiology 220 (3) (2001) 810–815.

[33] T. Yokoo, M. Bydder, G. Hamilton, et al., Nonalcoholic fatty liver disease: diagnostic and fat-grading accuracy of low-flip-angle multiecho gradient-recalled-echo MR imaging at 1.5 T, Radiology 251 (1) (2009) 67–76.

[34] T. Yokoo, M. Shiehmorteza, G. Hamilton, et al., Estimation of hepatic proton-density fat fraction by using MR imaging at 3.0 T, Radiology 258 (3) (2011) 749–759.

[35] S. Majumder, N.A. Philip, N. Takahashi, M.J. Levy, V.P. Singh, S.T. Chari, Fatty pancreas: should we be concerned? Pancreas 46 (10) (2017) 1251.

[36] V.F. Dalto, R.L. Assad, M.M. Lorenzato, M.D. Crema, P. Louzada-Junior, M.H. Nogueira-Barbosa, Comparison between STIR and T2-weighted SPAIR sequences in the evaluation of inflammatory sacroiliitis: diagnostic performance and signal-to-noise ratio, Radiol. Bras. 53 (2020) 223–228.

[37] L.W. Mann, D.M. Higgins, C.N. Peters, et al., Accelerating MR imaging liver steatosis measurement using combined compressed sensing and parallel imaging: a quantitative evaluation, Radiology 278 (1) (2016) 247–256.